JAMES | Journal of Advances in Modeling Earth Systems

RESEARCH ARTICLE
10.1029/2018MS001359

Improving AGCM Hurricane Structure With Two-Way Nesting

Kun Gao[1], Lucas Harris[2], Jan-Huey Chen[2,3], Shian-Jiann Lin[2], and Andrew Hazelton[1]

[1]The Program in Atmospheric and Oceanic Sciences, Princeton University, Princeton, NJ, USA, [2]NOAA Geophysical Fluid Dynamics Laboratory, Princeton, NJ, USA, [3]University Corporation for Atmospheric Research, Boulder, CO, USA

Key Points:
- Two-way nesting is an efficient way to better-resolve mesoscale features over a selected region in global models
- The regionally refined 8-km grid substantially improves the hurricane inner-core size and structure representations
- The realistic representation of inner-core inertial stability helps improve the simulated hurricane intensification processes

Correspondence to:
K. Gao,
kun.gao@noaa.gov

Citation:
Gao, K., Harris, L., Chen, J.-H., Lin, S.-J., & Hazelton, A. (2019). Improving AGCM hurricane structure with two-way nesting. *Journal of Advances in Modeling Earth Systems*, *11*, 278–292. https://doi.org/10.1029/2018MS001359

Received 26 APR 2018
Accepted 27 DEC 2018
Accepted article online 4 JAN 2019
Published online 25 JAN 2019

Abstract We demonstrate that two-way nesting significantly improves the structure of simulated hurricane in an atmospheric general circulation model. Two sets of 30-day hindcast experiments are conducted, one with the global-uniform-resolution (approximately 25-km nominal horizontal resolution) and the other with a regionally refined two-way nest (approximately 8 km over the tropical North Atlantic). The increase in the horizontal resolution on the nested grid improves the representation of storm intensity and intensification rate. When normalized by the radius of maximum wind (RMW), composite hurricane structures are generally similar in both simulations and compare well to observations. However, the hurricanes in the globally uniform configuration have much larger RMWs than observed, while those in the two-way-nested configuration have more realistic RMWs. We also find that the representation of the RMW has a critical impact on the simulation of inertial stability and boundary-layer convergence in the inner-core region. The more realistic inner-core size (indicated by RMW) and structure are possible reasons for the improved intensification rates in the two-way-nested configuration.

1. Introduction

Global climate models (GCMs) have made great improvements in the representation of global tropical cyclone (TC) climatology and variability in the past decade, benefiting most from the increased resolution and improved model dynamics and physical parameterizations. It has been demonstrated that atmospheric GCMs (AGCMs), when forced by the observed sea surface temperature (SST) field, can reproduce reasonable geographic distributions of TC genesis locations and tracks, as well as the interannual variability of basinwide TC counts (e.g., Zhao et al., 2009). Retrospective seasonal forecasts of hurricanes based on atmospheric GCMs (e.g., Chen & Lin, 2011, 2013) and atmosphere-ocean coupled GCMs (e.g., Murakami et al., 2015; Vecchi et al., 2014) showed promising skills in certain basins, particularly in the North Atlantic.

One obvious shortcoming of the majority of GCMs is that owing to their relatively coarse nominal horizontal resolution (typically 25 km or coarser), they are not capable of realistically representing the three-dimensional TC structure, which is critical in determining the TC intensity evolution. As identified in previous studies, a common issue for the coarse-resolution GCMs is that they generally struggle to capture the observed wind-pressure relationship and generate strong enough hurricanes (e.g., Manganello et al., 2012; Murakami et al., 2015; Roberts et al., 2015). There are a few studies showing that increasing the model resolution could lead to improvements in the representation of TC intensity as well as their kinematic and thermodynamic structure (Manganello et al., 2012; Murakami et al., 2015; Roberts et al., 2015; Zarzycki & Jablonowski, 2014). However, as these studies generally lack a comparison with observations, the realism of the hurricane structure in the simulations is still not clear.

Increased horizontal resolution has been shown to improve simulated physical processes and the realism of modeled structure (e.g., Fierro et al., 2009; Gopalakrishnan et al., 2011) in regional models. However, using resolutions fine enough to represent the hurricane inner-core structure (at least 10 km) in GCMs is still very challenging due to limited computer resources. The recently developed two-way global-to-regional nesting capability in the Geophysical Fluid Dynamics Laboratory (GFDL) Finite Volume Cubed-Sphere Dynamical Core (FV3) (Harris & Lin, 2013, 2014) presents an efficient way to locally reach such high resolutions while retaining the large-scale circulation of the parent global model. In this study, we will demonstrate that the two-way nesting method significantly improves the realism of simulated hurricane structure compared to globally uniform coarse-resolution simulations.

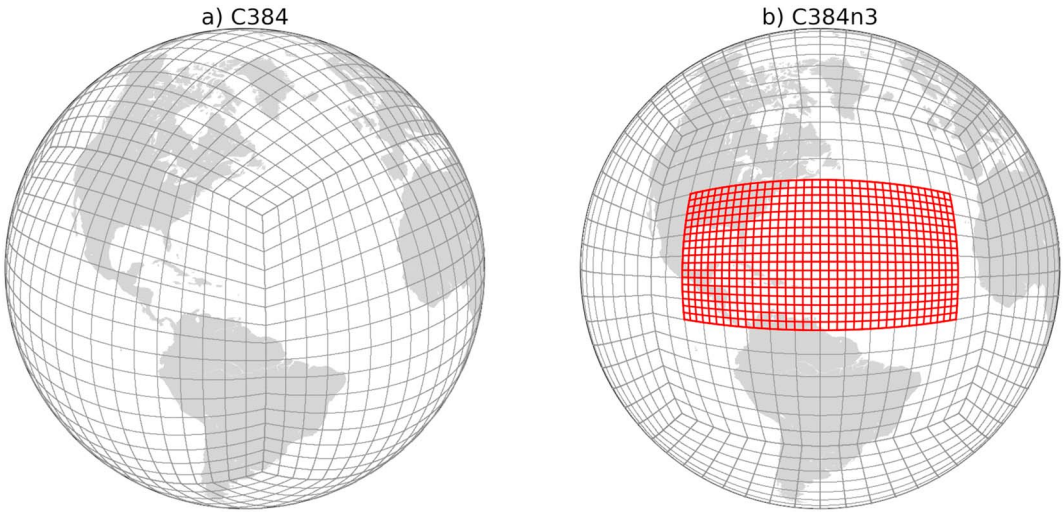

Figure 1. Two model grid configurations. (a) The cubed-sphere grid with approximately global-uniform 25-km horizontal resolution (labeled as C384). (b) A regional grid (the red mesh) two-way nested within the global grid with a refinement ratio of 3 (labeled as C384n3). Note that each plotted grid cell represents 24 by 24 actual grid cells.

2. Model and Data

2.1. Model Description

The GFDL High Resolution Atmospheric Model (HiRAM) has been used for investigating the climatology, variability, and seasonal prediction of hurricane activity (Chen & Lin, 2011, 2013; Held & Zhao, 2011; Zhao et al., 2010; Zhao & Held, 2012). In this study, we use the upgraded version of HiRAM used by Chen and Lin (2016) and Gao et al. (2017), which adopts the nonhydrostatic dynamics in FV3 and the double plume convection scheme of Zhao et al. (2016).

The two-way nesting method in FV3 was documented in Harris and Lin (2013), and here we only give a brief description of its design. The high-resolution nested grid covers a limited area of the global domain with horizontal boundaries aligned with the coarse-resolution global grid. The nested grid's boundaries are the coarse-grid solutions linearly interpolated in space and extrapolated in time, as the nested and coarse grids are integrated concurrently. To allow feedback from the nested grid onto the global grid, the coarse grid's wind and temperature solutions are periodically replaced with the spatially averaged nested grid solutions where the two grids coincide (Harris & Lin, 2013).

In this study, we analyze two sets of 30-day hindcast experiments, the first on a globally uniform 25-km grid and the other with the same global domain but with an 8-km nest over the tropical North Atlantic. Both sets of experiments produce a sufficiently large sample of storms to permit robust analysis of the simulated TC structure. The globally uniform and two-way nested grids are shown in Figure 1. The global-uniform-resolution grid configuration, called C384, uses a global cubed-sphere grid with 384 by 384 grid cells on each of the six tiles of the cube, which yields a grid-cell-width of approximately 25 km. In the global-to-regional nested configuration, called C384n3, the cubed-sphere grid is rotated to have a face covering the North Atlantic, centered around (60°W, 22.5°N); a factor-of-3 two-way nest is placed over North Atlantic, yielding approximately 8-km grid-cell width. The regional nest covers the area over which the North Atlantic TCs develop and make landfall. Although the 8-km horizontal resolution is not sufficiently high to realistically represent convective scale features (such as vortical hot towers) in TCs, we expect that it will lead to improvements in the mesoscale TC structure representation.

Table 1
Time Steps Used in the Two Grid Configurations

	C384	C384n3	
Time steps (second)		Global	Nested
Acoustic mode	28.5	25	10
Vertical remapping and tracer advection	200	200	100
Global-regional communication	—	200	200
Physical parameterizations	600	600	600

Both grids use identical sets of 63 Lagrangian vertical levels. The model top is set at 1 Pa, and the lowest model full level is about 30 m above the ocean surface. The time steps used in the two configurations are given in Table 1. The acoustic-mode time step used in the global grid (25 s) of the

C384n3 configuration is slightly smaller than that in the C384 configuration (28.5 s) to ensure numerical stability, but such difference is not expected to have any significant impacts on the large-scale circulation and TC structure simulations. We use same physical parameterizations in the two configurations to better reveal the impacts of increased resolution. Particularly, the same fourth-order divergence damping and vorticity damping (Lin & Harris, 2016) are applied in both grid configurations with identical settings, with nondimensional divergence and vorticity damping coefficients of 0.16 and 0.06, respectively.

For each configuration we ran a six-member ensemble of 30-day retrospective predictions, initialized on the first of each month from July to November in each of the years 2000–2014. Each ensemble member was initialized by adding small perturbations to the entrainment rate in the deep plume parameterization (Zhao et al., 2016). As in Chen and Lin (2013), the SST anomalies, calculated as the departure of the daily averaged SST field at initialization from the climatological SST in the corresponding month, were held constant throughout each 30-day run. In total, 450 thirty-day runs were conducted for each grid configuration. While a companion paper will evaluate the model prediction skill, this work examines the structural characteristics of the hurricanes formed in the two sets of simulations.

2.2. Model TC Analysis

2.2.1. Tracking and Selection

We apply the algorithm of Harris et al. (2016) to track the TCs in the model simulations. The TC tracking scheme detects all long-lived warm-core sea level pressure minima (see the appendix in Harris et al., 2016, for details). We define a tropical storm as a pressure minimum that lasts at least 72 hr (including the early tropical-depression stage), possesses a warm-core for at least 48 hr (not necessarily consecutive), and maintains a maximum 10-m wind of at least 17.5 m/s simultaneously with a warm-core for at least 36 consecutive hours. A hurricane is defined as any tropical storm that obtains a maximum 10-m wind of 33 m/s or greater while centered equatorward of 40° latitude. We select only the TCs that reached at least hurricane intensity in their lifetime in our analysis. Since the structures of TCs that exist at initialization are influenced by the initial conditions, we exclude these storms and focus only on the TCs formed by the model. We do not distinguish storms based on their formation time after initialization because we have not found any significant change in the TC characteristics during the monthlong simulations.

We focus on the TCs formed over North Atlantic basin, where the horizontal resolution is enhanced in the two-way-nested configuration. The characteristics of TCs in other basins in the C383n3 configuration are similar to those from the C384 configuration, which is expected since there is no change in the resolution over those regions. In total, 549 hurricanes over the North Atlantic from the 450 (six ensemble members combined) 30-day runs based on the C384 configuration, and 527 hurricanes from the C384n3 configuration, are selected.

2.2.2. Obtaining the Composite Axisymmetric Structure

The simulated hurricanes are composited to reveal their structural characteristics. We first extract the six-hourly atmospheric fields in a 12-degree by 12-degree box along the track of each selected TC. To obtain the TC wind field, we subtract the environmental wind, calculated as the averaged wind over the 12- by 12-degree area, from the total wind field. The horizontal TC wind fields are then projected onto storm-relative cylindrical coordinates to obtain the radial and tangential wind components, with the origin of the storm-relative cylindrical coordinates set to the grid point at which the TC wind speed has its smallest value. The axisymmetric structure is then obtained by performing azimuthal averaging, in which the radial bin width is set equal to the grid spacing. Each six-hourly azimuthally averaged snapshot is then mapped onto normalized radius r^*, which is the actual radius r divided by the radius of maximum wind (RMW). We define the RMW as the radius of maximum azimuthally averaged 10-m tangential wind. Unless otherwise stated, only TCs with maximum 10-m wind in the range of 33–60 m/s are used to create the composite. The upper intensity bound is selected based on the simulations in the C384 configuration (see section 3.3 for details).

2.3. TC Observational Data Sets

2.3.1. Extended Best Track

The TC track and intensity records over the years 1988–2015 are taken from the extended best track (EBT) data set (Demuth et al., 2006). In addition to the TC center location (latitude and longitude) and intensity (maximum 1-min sustained surface wind at 10-m height and minimum surface pressure) information, the

Table 2
Percentage Distributions of Hurricane Categories Based on Their Lifetime Maximum Intensity

Categories	Observations (%)	C384 (%)	C384n3 (%)
Category 1 (33.0–42.8 m/s)	30.5	59.1	27.2
Category 2 (42.8–49.5 m/s)	17.5	27.2	19.6
Category 3 (49.5–58.0 m/s)	20.3	11.7	19.9
Category 4 (58.0–70 m/s)	23.7	2.0	20.2
Category 5 (>70 m/s)	8.0	0.0	8.1

Note. The definition of categories follows the Saffir-Simpson Wind Scale.

EBT data set also provides an estimate of the RMW, which will be used for validating simulated RMW. It should be noted that the RMW parameter in the EBT data set is an operationally estimated parameter by National Hurricane Center forecasters based on aircraft reconnaissance or a combination of available satellite measurements. Although there is uncertainty in these estimated RMW records (especially for those further back in time), the EBT data set is the best available observational data set that contains RMW measurements for a large sample of hurricanes. Consistent with the criteria for selecting the simulated hurricanes, we only select hurricanes in the EBT data set formed from July to November; a total of 189 North Atlantic storms in the 28-year EBT data set are selected. On average, the number of selected storms in each year is about 6.8 in observations and 6.1 and 5.9 in each ensemble member of the C384 and C384n3 hindcast experiments, respectively. Table 2 summarizes the categorical distribution of all selected hurricanes based on their lifetime-maximum 10-m wind speed in observations and the two sets of model experiments.

2.3.2. GPS Dropsonde Observations

Following Zhang et al. (2011), we create azimuthal-height wind, temperature, and moisture composites in lower levels (below 2 km) based the long-term National Oceanic and Atmospheric Administration (NOAA) Global Positioning System (GPS) dropsonde data set of Wang (2015). This data set consists of a large sample (more than 13,000) of profiles obtained within 120 TCs over the years 1996–2012 in the North Atlantic and Northeast Pacific. For the purpose of this study, only the dropsonde observations taken under North Atlantic hurricanes with maximum 10-m wind speed from 33 to 60 m/s are selected. The RMW of the storm at the profile's observation time is linearly interpolated from two nearby RMW records in the EBT data set. In total 2,560 dropsonde profiles located within 5xRMW from 99 hurricanes are selected; spatial distributions are shown in Appendix A. These profiles are mapped to the same vertical levels with 30-m vertical resolution and then grouped as a function of r^* with a bin width set to 0.25xRMW. The final composite averaged data are smoothed using a 1-2-1 filter (repeated three times) in the radial direction only outside of 2xRMW.

2.3.3. Doppler Radar Observations

We also follow the procedures in previous studies (e.g., Reasor et al., 2013; Rogers et al., 2012) to create the wind composites throughout the entire depth of the troposphere based on Doppler radar observations. The data set used here contains observations taken from 22 different hurricanes over North Atlantic during the years 1997–2016 (Hazelton et al., 2018; Reasor et al., 2013; Rogers et al., 2012). The raw radar data were obtained in a three-dimensional swath (approximately 100-km width) along a flight leg through the TC. The three-dimensional wind vector was derived by solving the continuity and Doppler projection equations (Rogers et al., 2012). Most swaths have good coverage of the inner-core region. To get better spatial coverage, several flight legs (most flights had between 2 and 6 passes) were averaged to form a *merged analysis* (Rogers et al., 2013). For this study, only the observations taken under hurricanes with maximum 10-m wind speed from 33 to 60 m/s are considered. A total of 70 snapshots (one snapshot refers to one merged analysis) are selected. The processed data have a horizontal resolution of 2 km and a vertical resolution of 500 m with the lowest level at 500 m above the surface. Each snapshot is first azimuthally averaged and converted into an r^*-z coordinate system. The RMW is obtained based on the azimuthally averaged tangential wind at 500-m height. The 70 azimuthal-averaged radar snapshots are then averaged to create the TC wind composites.

3. Results

3.1. Intensity and Intensification Rate

Figure 2 shows the relationship between the maximum 10-m wind speed (V_{max}) and minimum surface pressure (P_{min}) of all hurricanes from the EBT data set and model simulations. Consistent with previous studies (e.g., Atkinson and Holliday, 1977; Landsea et al., 2004), we assume that the wind-pressure relationship can be written as

$$V_{max} = a(P_{ref} - P_{min})^b, \quad (1)$$

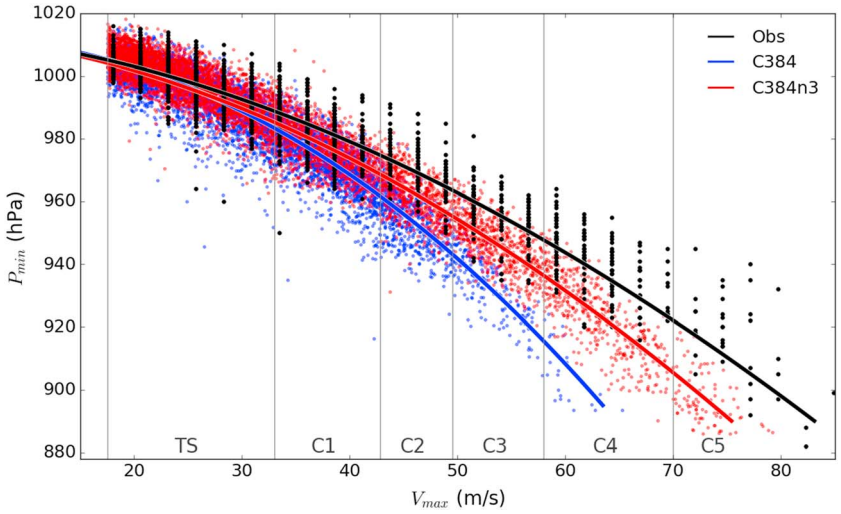

Figure 2. Wind-pressure relationship. The black dots are the six-hourly data points from observations; the blue dots are from the C384 simulations; the red dots are from the C384n3 simulations. The curves are the least squares fitted power function based on the scattered dots. C1–C5 represents Categories 1–5.

where the reference pressure, P_{ref}, is set to 1,013 hPa (same value as Landsea et al., 2004) for both model and observations and a and b are determined by a least squares fit. Similar to Landsea et al. (2004) and Knaff and Zehr (2007), we perform the fitting based on bin-averaged V_{max} and P_{min} in 2.5 m/s groups (17.5–20 m/s, 20–22.5 m/s, and so on) to weight the data points in the high intensity range equally to those in the low intensity range.

One noticeable difference between the two grid configurations is that the C384n3 configuration generates more major hurricanes (Category 3 and above; lifetime V_{max} greater than 49.5 m/s) than the C384 configuration. Nearly 48% of all hurricanes (Table 2) that formed in the C384n3 configuration were able to obtain major hurricane intensity, which is close to the percentage in observations (52%). By comparison, only 11.9% of all hurricanes reached major hurricane intensity in the C384 configuration. This indicates that the increase in resolution allows the modeled hurricanes to reach a stronger lifetime maximum intensity, which is consistent with previous studies (e.g., Manganello et al., 2012; Murakami et al., 2015).

Figure 2 indicates that the TCs in the C384 configuration have much weaker V_{max} at a given P_{min} than is observed, which becomes more apparent as the intensity increases. The increased resolution in the C384n3 configuration substantially improves the wind-pressure relationship, especially in the high wind speed regime ($V_{max} > 50$ m/s). Chavas et al. (2017) suggested that the central pressure deficit (measured by the difference between the environmental pressure and the TC central pressure) is mainly related to the TC maximum wind speed and storm size as well as the Coriolis parameter; as shown below the improved wind-pressure relationship in the C384n3 configuration is likely due to the improvement in the representation of storm size. The C384n3 configuration still produces weaker V_{max} under a given P_{min} than as observed. This could be because the model resolution is not sufficiently high, or there is deficiency in the surface drag parameterization under high wind speed conditions. Further work will be focused on further improving the wind-pressure relation in the C384n3 configuration.

We next examine the TC intensity evolution in the two sets of simulations. Previous studies suggest that the TC intensification rate is critically affected by the simulated storm structure. We first determine intensification periods for all selected storms in both observations and model simulations, and then calculate the intensification rate, measured by 24-hr change in V_{max}. Figure 3 shows the histograms of the intensification rate records from both grid configurations compared to observations. The distribution in the C384 configuration (Figure 3a) indicates that the model storms are generally characterized by low intensification rates compared to those in observations. Only 28.7% of hurricanes formed in the C384 simulations went through rapid intensification (RI; defined as the event when the 24-hr V_{max} change

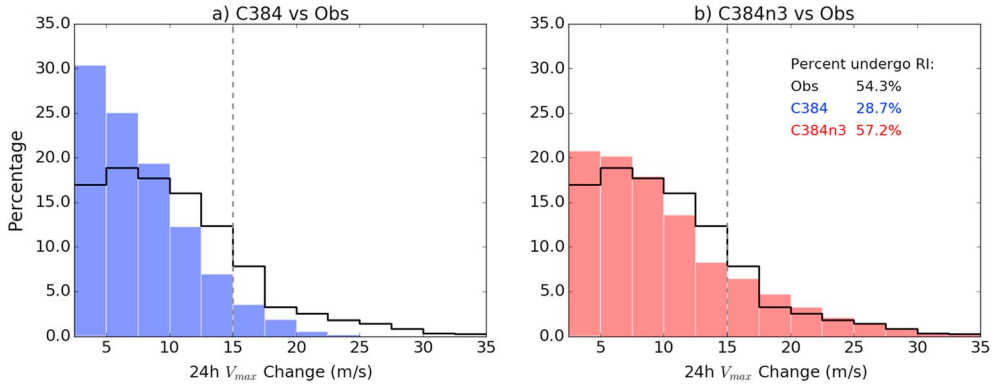

Figure 3. Histograms of 24-hr change in maximum 10 m wind (V_{max}) for all intensifying hurricanes in (a) C384 and (b) C384n3 simulations. The black line in (a) and (b) shows the histogram in observations for reference. The gray dashed line indicate the threshold of the rapid intensification (RI) event. The percentage of total hurricanes that underwent RI in observations and the two sets of model simulations are shown in (b).

exceeds 15.4 m/s) in their lifetime, a percentage much smaller than in observations (54.3%). In contrast, the C384n3 configuration produces a more realistic distribution of the 24-hr V_{max} change (Figure 3b) and ratio of storms that underwent RI (57%).

The above analysis indicates the higher resolutions achieved through two-way nesting leads to substantial improvements in the representation of storm lifetime maximum intensity and intensification rate. There is no significant difference in the simulated large-scale environment (vertical wind shear between 200 and 850 hPa, midlevel moisture, etc.) between the two grid configurations (not shown). Considering that the physical parameterizations used in the two set of configurations are the same, the above results suggest that the increased horizontal resolution in the C384n3 configuration improves the representation of storm-scale structure and intensification processes.

3.2. Radius of Maximum Wind

In this section, we examine the values of RMW, which is often used to indicate the TC inner-core size, in the two sets of configurations. The definition of inner-core region varies in the literature. Here we define the inner-core region as the annular area between 0.5 and 2.5 RMW, an area that includes the eyewall but excludes the eye region. The storm structure and physical processes in the inner-core region have been recognized as being critical for intensification (e.g., Paull et al., 2017; Schubert & Hack, 1982; Smith & Montgomery, 2016; Vigh & Schubert, 2009). The observed RMW for a mature hurricane typically ranges from 20 to 60 km (Figure 4), which can only be marginally resolved by a 25-km grid-cell width model. It

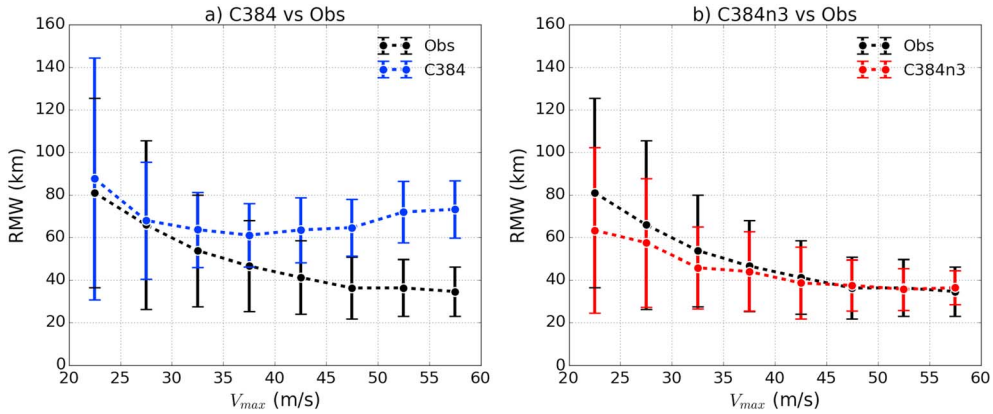

Figure 4. Bin-averaged radius of maximum wind (RMW) as a function of maximum 10-m wind speed (V_{max}). The bin averaging is performed in consecutive 5 m/s intensity brackets. The bar indicates 1 standard deviation in each 5 m/s intensity bin.

is thus expected that the horizontal resolution will have a direct impact on the RMW of modeled hurricanes.

To illustrate the change of RMW with intensity, we obtain the bin-averaged RMW of all intensifying storms in consecutive 5 m/s intensity bins (20–25 m/s, ..., 55–60 m/s). The maximum intensity range is set to 55–60 m/s because there are too few hurricanes with V_{max} greater than 60 m/s in the C384 simulations (Figure 2). As shown in Figure 4, both the mean value and the standard deviation of RMW decrease with the increase of intensity in observations, suggesting that the storm intensification is accomplished through the contraction of the inner core. The bin-averaged RMW in observations seems to gradually reach a uniform value of slightly less than 40 km as V_{max} becomes larger than 45 m/s.

Although the C384 configuration reasonably captures the RMW in the low intensity regime (Figure 4a; V_{max} smaller than 30 m/s), in the hurricane intensity regime the mean values of RMW are overall much larger than observed, and do not get appreciably smaller than 60 km. The departure from the observed value increases with increasing intensity. For storms with V_{max} greater than 50 m/s, the mean RMW in C384 simulations is about twice larger than observed. This deficiency of the C384 configuration is not surprising considering that the modeled TCs cannot have RMW smaller than the width of two grid cells and observed mean RMW in the hurricane intensity range (approximately 40 km) is less than the width of two C384 grid cells. It is interesting that the bin-averaged RMW increases as V_{max} becomes larger than 40 m/s in the C384 configuration, which is associated with an outward shift of the eyewall and maximum precipitation rate (not shown). The physical mechanism behind the expansion of the inner-core region in more intense storms (V_{max} greater than 40 m/s) in the C384 configuration remains unclear and warrants future investigation.

Intuitively, increasing the horizontal resolution should allow the model TCs to develop smaller RMWs. Consistent with observations, the RMW in the C384n3 simulations (Figure 4b) decreases with intensity on average and gradually approaches a uniform value for the most intense storms. The bin-averaged RMW in the C384n3 simulations closely agrees with observations in the hurricane intensity range (Figure 4b). Beyond the wind speed range shown in Figure 4, the observed RMW continues to decrease slightly with intensity but remains larger than 25 km, and the C384n3 configuration is still in reasonable agreement with observations (not shown).

The difference in RMW between the two sets of simulations indicates that the hurricanes formed in the C384 configuration are characterized by much broader inner-core region than in the C384n3 configuration. The implications of RMW and thereby inner-core size on inner-core structure and storm intensification will be discussed in sections 3.4 and 3.5.

3.3. Composite Axisymmetric Structures

In this section, we compare the composite axisymmetric hurricane structures from the two sets of simulations and compare them to composites derived from radar and GPS dropsonde observations. Since hurricane structure is dependent on its intensity, to reveal the impact the horizontal resolution on the hurricane structure, we create composites from snapshots in the same V_{max} range (33–60 m/s).

Figure 5 shows the composites of the azimuthal-averaged tangential (V), radial (U), and vertical (W) winds on the r^*-z coordinates obtained from the two model configurations and radar observations. The two configurations have rather similar tangential wind distribution, despite the fact that the RMW in the C384 configuration is overall significantly larger than that in the C384n3 configuration. The hurricanes from both configurations are characterized by reasonable secondary flow structure: shallow radial inflow in the boundary layer (BL), a broad outflow in the upper levels (approximately 10–16 km), and a well-defined eyewall updraft that originates inside of the RMW near the surface and slopes outward with height.

Figure 6 shows the composite wind and thermodynamic fields below 2 km from model simulations and GPS dropsonde observations. The dropsonde composites created in this study are broadly consistent with Zhang et al. (2011). Both grid configurations reasonably captured the main features in the observed BL structure, although the agreements are not perfect. Consistent with the observations, the maximum tangential wind

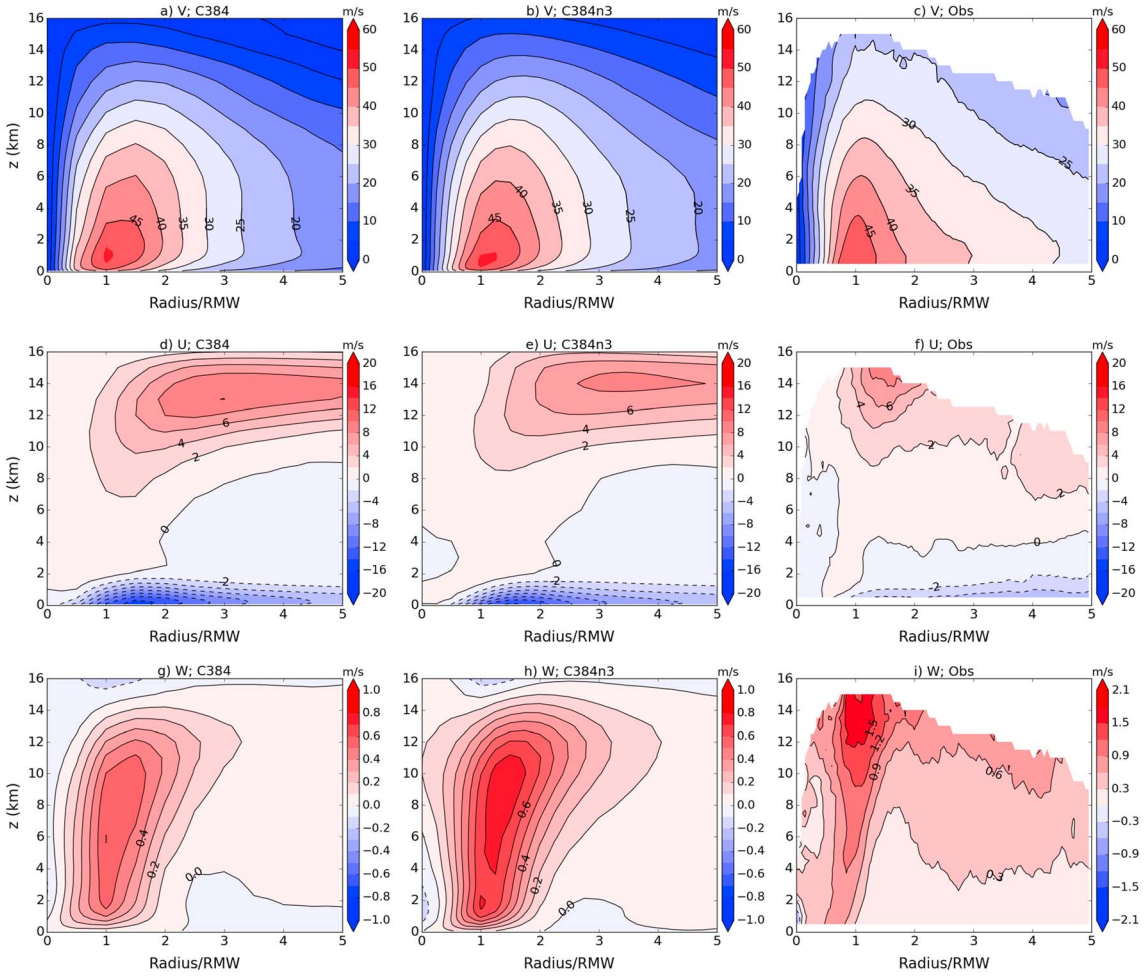

Figure 5. Radius-vertical cross sections of the composite (a–c) tangential, (d–f) radial, and (g–i) vertical winds from (left to right) the C384 configuration, C384n3 configuration, and radar observations. The individual snapshots used for creating the composites are in the same intensity range: 33–60 m/s. The radius is normalized by the radius of maximum wind (RMW), which in average is about 68, 40, and 45 km for C384, C384n3, and radar observations, respectively. In the radar composites (c, f, and i), the grid points without sufficient samples (less than 30) are masked out. To better show the distribution of the vertical velocities in the model simulations, we use a smaller colorbar range in Figures 5g and 5h than in Figure 5i.

in both model composites occurs in the mid-BL within the radial inflow layer. The two grid configurations also captured reasonable radial inflow distributions, as well as the presence of the weak radial outflow immediately aloft. The temperature and the specific humidity fields in both grid configurations are also in good agreement with observations.

There are some notable inconsistencies between the model and observed composites. The tangential wind in both model configurations weakens faster along the normalized radius than observed (Figures 5a–5c and 6a–6c), which might due to insufficient outer-region rainband activity in the model. Also, the eyewall updrafts in both configurations are weaker than in observations (Figures 5g, 5h, and 5f), which is likely because neither grid's resolution is fine enough to realistically represent the intense convective bursts in the inner-core region. The vertical velocity in the radar composite (Figure 5f) reaches its maximum value near the tropopause, higher than in the model composites (Figures 5g and 5h). It remains unclear if such inconsistency is due to model deficiency or errors in the vertical velocity measurements. Despite these deviations from the observed composite, we are still confident that the broader agreement in both model versions with the observed composites implies that both configurations give a realistic axisymmetric dynamical and thermodynamic structure along normalized radius. In the following sections, we examine the differences in the inner-core structure between the two grid configurations.

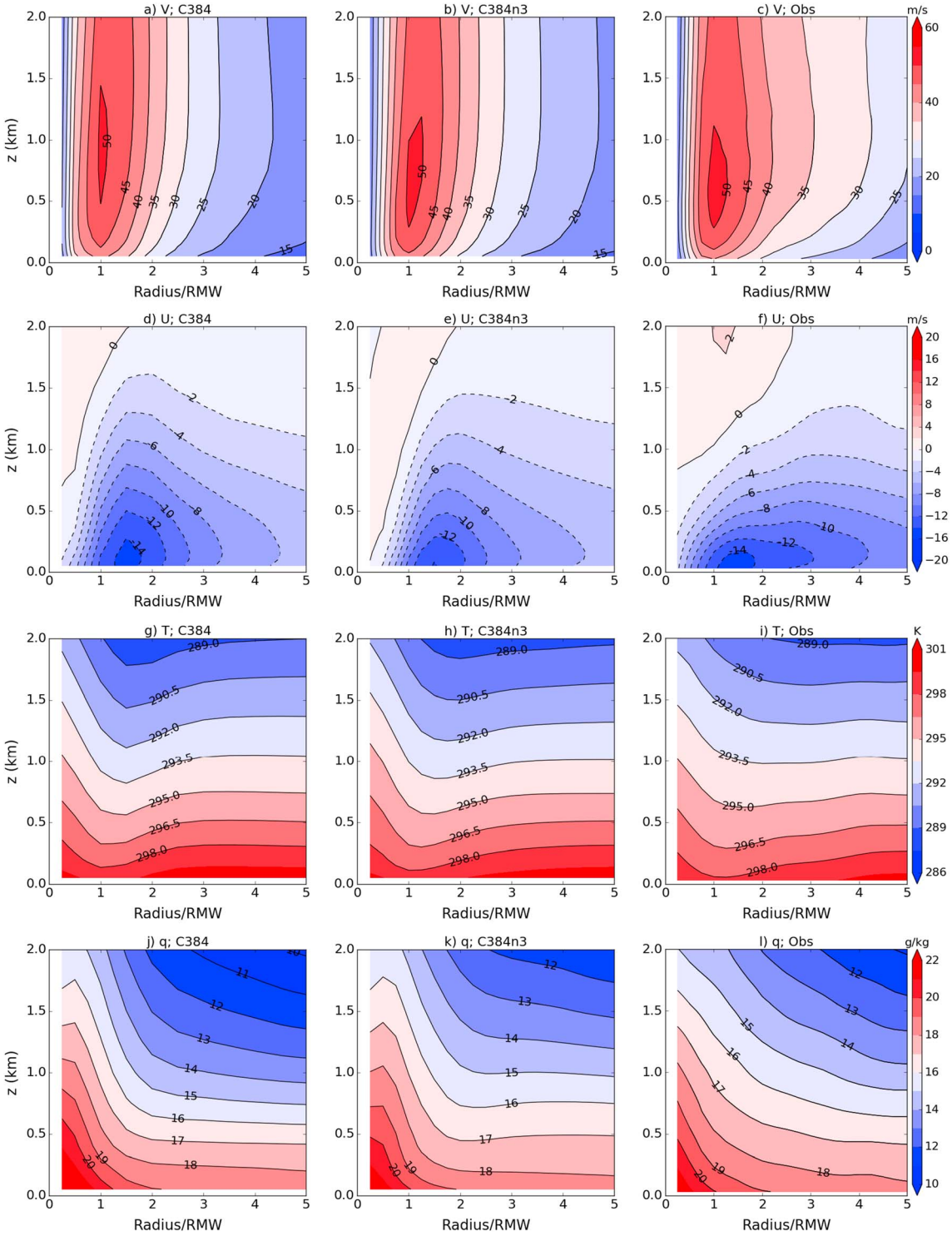

Figure 6. Radius-vertical cross sections of the composite (a–c) tangential wind, (d–f) radial wind, (g–i) temperature, and (j–l) specific humidity from (left to right) the C384 configuration, the C384n3 configuration, and GPS dropsonde observations. The intensity range is 33–60 m/s. The radius is normalized by the radius of maximum wind (RMW), which in average is 68, 40, and 39 km for C384, C384n3, and dropsonde observations, respectively.

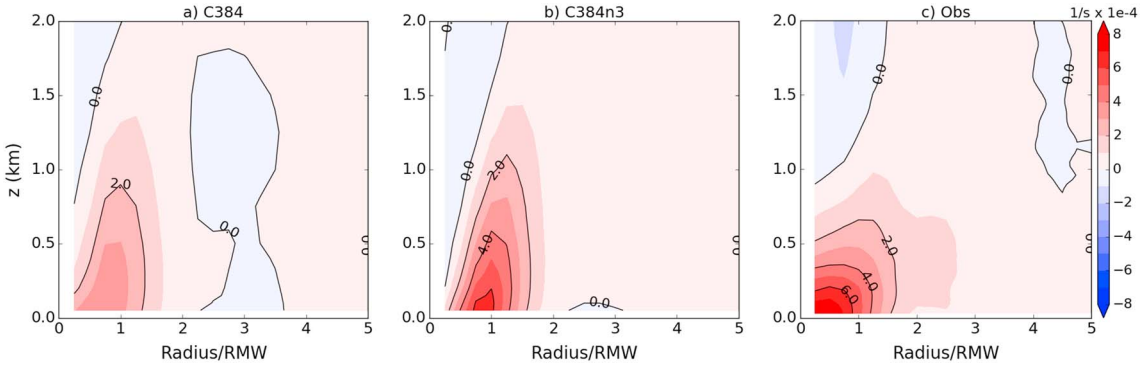

Figure 7. Same as Figure 6 but for the radial convergence.

3.4. Boundary Layer Convergence and Eyewall Convection

The eyewall updrafts in the C384n3 configuration (Figure 5h) are noticeably stronger than in the C384 configuration (Figure 5g). We will show that such difference is related to the difference in the inner-core size (RMW).

For an axisymmetric TC, the horizontal convergence is only dependent upon the radial component of the wind and can be written as

$$-\left(\frac{U}{r}+\frac{\partial U}{\partial r}\right), \tag{2}$$

where U is the azimuthally averaged radial wind. Figure 7 shows composites of horizontal convergence obtained from both sets of model simulations and observations. It should be noted that while the model composites (Figures 7a and 7b) are obtained by averaging individual snapshots of the convergence field, the observed convergence (Figure 7c) is obtained based on the U composite obtained from GPS dropsonde profiles (Figure 6f). Consistent with observations, both model configurations show that the maximum convergence occurs inside the RMW near the surface and coincides with the eyewall updraft. However, the C384 configuration underrepresents the magnitude of the convergence, particularly near the base of the eyewall updraft, while the convergence in the C383n3 configuration is closer to observations.

The difference in the convergence in the two grid configurations can be explained by the difference in RMW. Since radial wind distributions as a function of *normalized* radius in the two grid configurations (Figures 6d and 6e) are similar, stronger convergence near the base of the eyewall updraft is favored when RMW is smaller, since both factors in (2) are larger. Previous studies (e.g., Kepert & Nolan, 2014) indicated that BL convergence modulates the radial location and strength of the eyewall updraft. The stronger BL convergence resulting from a smaller RMW provides an explanation for the stronger eyewall updrafts (Figure 5) in the C384n3 configuration.

3.5. Inertial Stability and Hurricane Intensification

The inertial stability parameter (I) in the inner-core region is a critical parameter that affects the hurricane intensification rate (Paull et al., 2017; Schubert & Hack, 1982; Smith & Montgomery, 2016; Vigh & Schubert, 2009). The definition of I is given as

$$I^2=(f_0+\zeta)\cdot\left(f+\frac{2V}{r}\right), \tag{3}$$

where f_0 is the Coriolis parameter at the storm center (assuming the variation of the Coriolis parameter within a storm is negligible), V is the azimuthally averaged tangential wind, r is the radius, and ζ is the vertical component of the relative vorticity given by

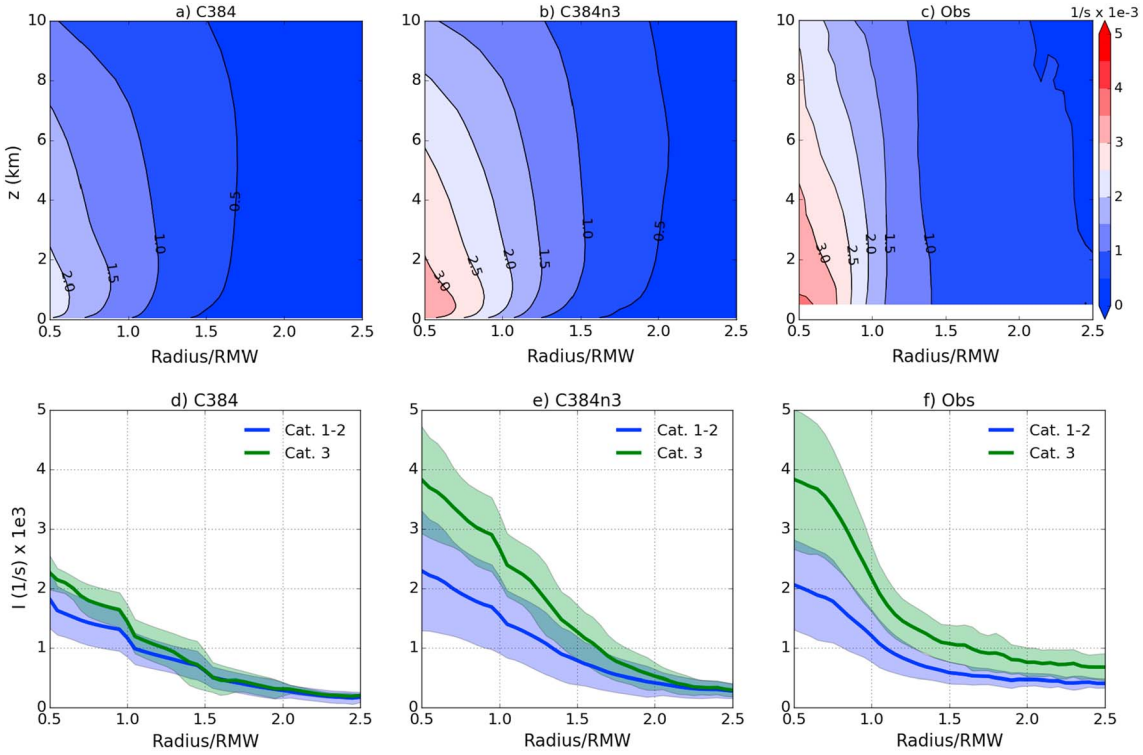

Figure 8. (a–c) Same as Figure 5 but for the composite inertial stability parameter. (d–f) The radial distribution of the inertial stability parameter at 2-km height from (left to right) C384, C384n3, and radar observations, respectively; the blue line shows the composite for the Categories 1–2 (33–49.5 m/s) hurricanes, and the green line shows Category 3 (49.5–58 m/s) hurricanes. The shading indicates 1 standard deviation.

$$\zeta = \frac{V}{r} + \frac{\partial V}{\partial r}. \tag{4}$$

In the inner-core region, a larger value of I often implies a larger value of ζ, and vice versa.

From the definition of I it is obvious that a larger RMW implies a smaller I in the inner-core region. We expect the hurricanes formed in the C384 configurations to be characterized by weaker I in the inner-core region than those in the C384n3 configuration. Figure 8 shows the composite I in the inner-core region obtained from the model simulations and radar observations: hurricanes from the C384 simulations are characterized by a much smaller I near RMW than observed, largely due to the unrealistically large RMWs. In contrast, hurricanes from C384n3 have much better agreement with observations. Figures 8d–8f show composite I profiles at 2-km height in two intensity ranges: Categories 1–2 (33–49 m/s) and Category 3 (49–58 m/s). In the radar observations, there is significant difference between I composites in the two intensity ranges, which is due to the increase in wind speed and the reduction of RMW. The C383n3 configuration reasonably captures such changes and the value of I near RMW agrees with observations. However, the C384 configuration failed to capture the substantial change in I due to the significant RMW bias in the major hurricane intensity regime (Figure 4). Both configurations produce smaller I than observed in the outer region (radius greater than 2x RMW; not shown) due to the bias in the tangential wind (Figures 5a–5c and 6a–6c).

The magnitude of I in the inner-core region has significant impact on the hurricane intensification rates, measured by the increase in the tangential wind speed. It has been widely accepted that a larger I in the region of the eyewall convection, which exists near the RMW in both configurations as well as observations and other high-resolution models, provides a more favorable environment for storm intensification. Traditionally, it has been argued that under a given fixed diabatic heating source, a larger I promotes more efficient warming of the rising air, and therefore more efficient spin-up of tangential

wind through thermal wind balance (Schubert & Hack, 1982; Vigh & Schubert, 2009). Alternatively, recent studies (Paull et al., 2017; Smith & Montgomery, 2016) suggest that the role of I in storm intensification can be understood in view of the radial transport of vorticity (or equivalently, the radial transport of angular momentum): a larger I in the inner-core region implies a larger ζ, and thus an enhanced inward radial transport of vorticity, which leads to enhanced intensification. Both arguments conclude that a larger I is favorable for hurricane intensification. The difference in I shown in Figure 7 is at least partially responsible for the observed intensification difference (Figure 3). A realistic representation of RMW and I is the possible reasons for the realistic representation of intensification rates in the C384n3 configuration.

It should be noted that the TC intensification is a complicated process that involves interactions between physical processes at multiple scales and is also affected by model parameterizations. There could be other possible reasons for the intensification rate differences between the two grid configurations besides the change in the inner-core inertial stability identified above. For example, it was shown that reducing the horizontal diffusion could significantly reduce the inner-core size and increase the storm intensity in an axisymmetric model (Bryan, 2012; Rotunno & Bryan, 2012). The nondimensional horizontal damping coefficients are dependent on the minimum grid-cell area (Lin & Harris, 2016). It is possible that the changes of damping coefficients with horizontal resolution contributed to the differences in RMW and intensification rate between the C384 and C384n3 configurations, which are not examined in the present study.

4. Summary

We analyzed the characteristics of simulated hurricanes in a suite of 30-day globally uniform and two-way-nested GFDL HiRAM simulations. We demonstrated that the locally enhanced resolution from the two-way nesting method significantly improves the representation of several fundamental aspects of the hurricane, particularly the hurricane inner-core structure, based on a comparison between large samples of simulated hurricanes and of observed hurricanes.

We first demonstrated that the increased horizontal resolution by the two-way nesting method leads to substantial improvements in the representation of hurricane intensity and intensification rate. The hurricanes from the global-uniform-resolution and two-way-nested simulations have similar composite wind and thermodynamic structure on the normalized radius (radius divided by RMW), and both grid configurations captured the gross features seen in observations. However, the two grid configurations differ substantially in the representation of hurricane RMW and thereby of inner-core size. The globally uniform-resolution configuration produces hurricanes that have much larger RMW than observed due to insufficient resolution. The two-way-nested configuration overcomes this deficiency and produces hurricanes with RMW in good agreement with observations.

Further analyses indicate that better representation of RMW has important impacts on the hurricane inner-core structure. The hurricanes in the two-way-nested configuration are characterized by larger inertial stability in the inner-core region and stronger BL convergence that promote more intense eyewall convection than those in the globally uniform-resolution configuration. The improved representations of RMW, inertial stability and BL convergence likely act in concert to improve the representation of the storm intensification rate in the two-way-nested configuration.

This study demonstrates that the two-way-nesting method provides an efficient way for obtaining hurricane-resolving resolution over a selected region in the global model, which brings new opportunities for regional hurricane research based on GCMs. GCMs have previously been used to study the variability and project the future change of basin-wide hurricane frequency. The use of the two-way nesting in GCMs will allow research on impacts and characteristics related to finer-scale vortex features and structure. In particular, the wind, flood, and storm-surge damage caused by hurricanes are not only related to their intensity but also their size. The capacity of the two-way-nested configuration to capture the storm inner-core size and structure shows its potential for predictions of the hurricane damage on subseasonal-to-seasonal scale as well as for changes in hurricane damage under external forcing or due to climate variability.

Appendix A: GPS Dropsonde Observations

Figure A1 shows the geographic distribution of the selected dropsonde profiles used for creating the BL composites. Figure A2 shows the location of the selected dropsonde profiles relative to the storm center. The observations are approximately evenly distributed along the azimuthal direction at a given radius. The majority of profiles were obtained near the RMW.

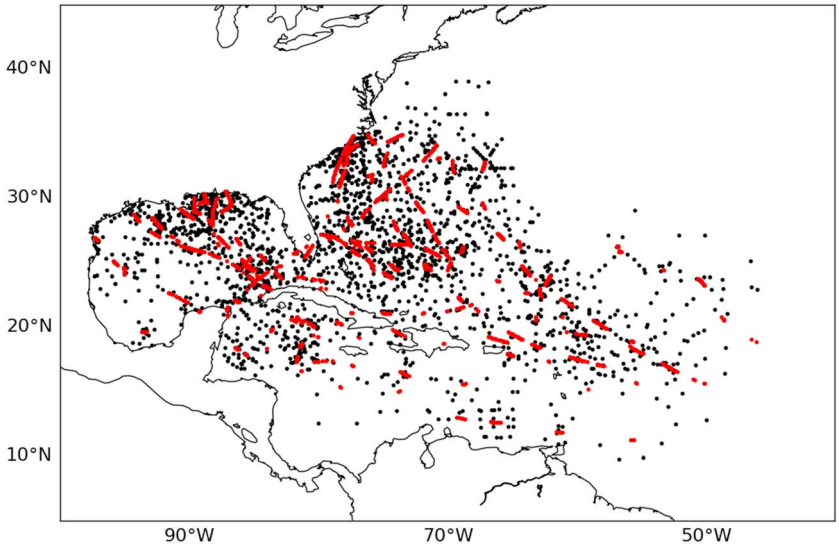

Figure A1. Locations of the dropsonde profiles (black) and the storm centers (red).

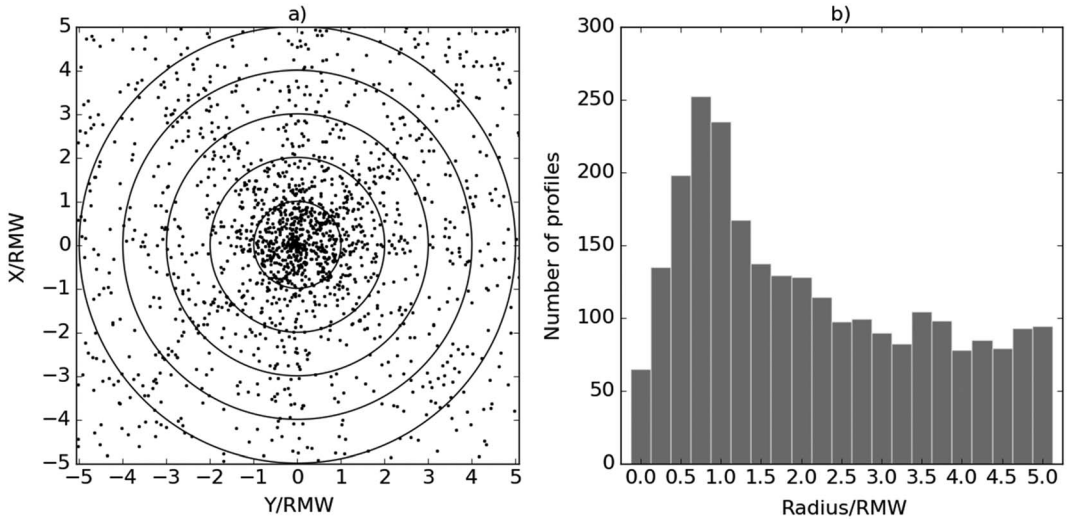

Figure A2. (a) Locations of dropsonde profiles relative to the storm center. The eastward and northward distances from the storm center are normalized by the radius of maximum wind (RMW). The black circles indicate the distance from the center with an interval of 1 RMW. (b) The count of dropsonde profiles in each 0.25 RMW bin. The RMW is approximately 39 km in average.

Acknowledgments

We thank Morris Bender, Steve Garner, and Yongqiang Sun for valuable discussions. We also thank the Associate Editor David Nolan and three anonymous reviewers for providing helpful comments that improved this manuscript. This research was supported under award NA14OAR4830101 from the National Oceanic and Atmospheric Administration (NOAA), U.S. Department of Commerce. The statements, findings, conclusions, and recommendations are those of the author(s) and do not necessarily reflect the views of the National Oceanic and Atmospheric Administration or the U. S. Department of Commerce. We thank NOAA Atlantic Oceanographic and Meteorological Laboratory/Hurricane Research Division for providing the Doppler radar observations and the staff of NOAA Aircraft Operation Center who have collected the radar data over many years. The Extended Best Track data set is available at http://rammb.cira.colostate.edu/research/tropical_cyclones/tc_extended_best_track_dataset/. The long-term NOAA Dropsonde Hurricane Archive is available at https://data.eol.ucar.edu/dataset/542.001. All model data used in this work are stored through NOAA/GFDL Archiving System at the location/archive/Kun.Gao/DATA/2018_JAMES_TC.

References

Atkinson, G. D., & Holliday, C. R. (1977). Tropical cyclone minimum sea level pressure/maximum sustained wind relationship for the western North Pacific. *Monthly Weather Review*, *105*, 421–427.

Bryan, G. H. (2012). Effects of surface exchange coefficients and turbulence length scales on the intensity and structure of numerically simulated hurricanes. *Monthly Weather Review*, *140*(4), 1125–1143. https://doi.org/10.1175/MWR-D-11-00231.1

Chavas, D. R., Reed, K. A., & Knaff, J. A. (2017). Physical understanding of the tropical cyclone wind–pressure relationship. *Nature Communications*, *8*(1), 1360. https://doi.org/10.1038/s41467-017-01546-9

Chen, J.-H., & Lin, S.-J. (2011). The remarkable predictability of inter- annual variability of Atlantic hurricanes during the past decade. *Geophysical Research Letters*, *38*, L11804. https://doi.org/10.1029/2011GL047629

Chen, J.-H., & Lin, S.-J. (2013). Seasonal predictions of tropical cyclones using a 25-km-resolution general circulation model. *Journal of Climate*, *26*(2), 380–398. https://doi.org/10.1175/JCLI-D-12-00061.1

Chen, J.-H., & Lin S.-J. (2016). Seasonal prediction of tropical cyclones in a new non-hydrostatic GFDL HiRAM, *32nd Conference on Hurricanes and Tropical Meteorology*, San Juan, PR, Amer. Meteor. Soc., 3C.3. (Available online at https://ams.confex.com/ams/32Hurr/webprogram/Paper293909.html)

Demuth, J., DeMaria, M., & Knaff, J. A. (2006). Improvement of advanced microwave sounder unit tropical cyclone intensity and size estimation algorithms. *Journal of Applied Meteorology*, *45*(11), 1573–1581. https://doi.org/10.1175/JAM2429.1

Fierro, A. O., Rogers, R. F., Marks, F. D., & Nolan, D. S. (2009). The impact of horizontal grid spacing on the microphysical and kinematic structures of strong tropical cyclones simulated with the WRF-ARW model. *Monthly Weather Review*, *137*(11), 3717–3743. https://doi.org/10.1175/2009MWR2946.1

Gao, K., Ginis, I., Doyle, J., & Jin, Y. (2017). Effect of boundary layer roll vortices on the development of an axisymmetric tropical cyclone. *Journal of the Atmospheric Sciences*, *74*(9), 2737–2759. https://doi.org/10.1175/JAS-D-16-0222.1

Gopalakrishnan, S. G., Marks, F. D., Zhang, X., Bao, J.-W., Yeh, K.-S., & Atlas, R. (2011). The experimental HWRF system: A study on the influence of horizontal resolution on the structure and intensity changes in tropical cyclones using an idealized framework. *Monthly Weather Review*, *139*(6), 1762–1784. https://doi.org/10.1175/2010MWR3535.1

Harris, L. M., & Lin, S.-J. (2013). A two-way nested global-regional dynamical core on the cubed-sphere grid. *Monthly Weather Review*, *141*(1), 283–306. https://doi.org/10.1175/MWR-D-11-00201.1

Harris, L. M., & Lin, S.-J. (2014). Global-to-regional nested-grid climate simulations in the GFDL High Resolution Atmosphere Model. *Journal of Climate*, *27*(13), 4890–4910. https://doi.org/10.1175/JCLI-D-13-00596.1

Harris, L. M., Lin, S.-J., & Tu, C. Y. (2016). High resolution climate simulations using GFDL HiRAM with a stretched global grid. *Journal of Climate*, *29*(11), 4293–4314. https://doi.org/10.1175/JCLI-D-15-0389.1

Hazelton, A. T., Harris, L., & Lin, S.-J. (2018). Evaluation of tropical cyclone structure forecasts in a high-resolution version of the multi-scale GFDL FVGFS model. *Weather and Forecasting*, *33*(2), 419–442. https://doi.org/10.1175/WAF-D-17-0140.1

Held, I. M., & Zhao, M. (2011). The response of tropical cyclone statistics to an increase in CO2 with fixed sea surface temperatures. *Journal of Climate*, *24*(20), 5353–5364. https://doi.org/10.1175/JCLI-D-11-00050.1

Kepert, J. D., & Nolan, D. S. (2014). Reply to "Comments on 'How does the boundary layer contribute to eyewall replacement cycles in axisymmetric tropical cyclones?'". *Journal of the Atmospheric Sciences*, *71*(12), 4692–4704. https://doi.org/10.1175/JAS-D-14-0014.1

Knaff, J. A., & Zehr, R. M. (2007). Reexamination of tropical cyclone wind–pressure relationships. *Weather Forecasting*, *22*, 71–88. https://doi.org/10.1175/WAF965.1

Landsea, C. W., Anderson, C., Charles, N., Clark, G., Dunion, J., Fernandez-Partagas, J., et al. (2004). The Atlantic hurricane database re-analysis project: Documentation for the 1851-1910 alterations and additions to the HURDAT database. In R. J. Murname & K.-B. Liu (Eds.), *Hurricanes and typhoons: Past, present and future* (pp. 177–221). Columbia University Press.

Lin, S.-J., & Harris, L. M. (2016). Explicit diffusion in GFDL FV3. Technical document Available at: https://www.gfdl.noaa.gov/wp-content/uploads/2017/09/Diffusion_operators.pdf

Manganello, J. V., Hodges, K. I., Kinter, J. L., Cash, B. A., Marx, L., Jung, T., et al. (2012). Tropical cyclone climatology in a 10-km global atmospheric GCM: Toward weather-resolving climate modeling. *Journal of Climate*, *25*(11), 3867–3893. https://doi.org/10.1175/JCLI-D-11-00346.1

Murakami, H., Vecchi, G., Underwood, S., Delworth, T., Wittenberg, A., Anderson, W., et al. (2015). Simulation and prediction of category 4 and 5 hurricanes in the high-resolution GFDL HiFLOR coupled climate model. *Journal of Climate*, *28*(23), 9058–9079. https://doi.org/10.1175/JCLI-D-15-0216.1

Paull, G., Menelaou, K., & Yau, M. K. (2017). Sensitivity of tropical cyclone intensification to axisymmetric heat sources: The role of inertial stability. *Journal of the Atmospheric Sciences*, *74*, 2325–2340.

Reasor, P. D., Rogers, R. F., & Lorsolo, S. (2013). Environmental flow impacts on tropical cyclone structure diagnosed from airborne Doppler radar composites. *Monthly Weather Review*, *141*(9), 2949–2969. https://doi.org/10.1175/MWR-D-12-00334.1

Roberts, M. J., Vidale, P. L., Mizielinski, M. S., Demory, M.-E., Schiemann, R., Strachan, J., et al. (2015). Tropical cyclones in the UPSCALE ensemble of high-resolution global climate models. *Journal of Climate*, *28*(2), 574–596. https://doi.org/10.1175/JCLI-D-14-00131.1

Rogers, R., Lorsolo, S., Reasor, P., Gamache, J., & Marks, F. (2012). Multiscale analysis of tropical cyclone kinematic structure from airborne Doppler radar composites. *Monthly Weather Review*, *140*(1), 77–99. https://doi.org/10.1175/MWR-D-10-05075.1

Rogers, R., Reasor, P., & Lorsolo, S. (2013). Airborne Doppler observations of the inner-core structural differences between intensifying and steady-state tropical cyclones. *Monthly Weather Review*, *141*(9), 2970–2991. https://doi.org/10.1175/MWR-D-12-00357.1

Rotunno, R., & Bryan, G. H. (2012). Effects of parameterized diffusion on simulated hurricanes. *Journal of the Atmospheric Sciences*, *69*(7), 2284–2299. https://doi.org/10.1175/JAS-D-11-0204.1

Schubert, W. H., & Hack, J. J. (1982). Inertial stability and tropical cyclone development. *Journal of the Atmospheric Sciences*, *39*(8), 1687–1697. https://doi.org/10.1175/1520-0469(1982)039<1687:ISATCD>2.0.CO;2

Smith, R. K., & Montgomery, M. T. (2016). The efficiency of diabatic heating and tropical cyclone intensification. *Quarterly Journal of the Royal Meteorological Society*, *142*(698), 2081–2086. https://doi.org/10.1002/qj.2804

Vecchi, G. A., Delworth, T., Gudgel, R., Kapnick, S., Rosati, A., Wittenberg, A. T., et al. (2014). On the seasonal forecasting of regional tropical cyclone activity. *Journal of Climate*, *27*(21), 7994–8016. https://doi.org/10.1175/JCLI-D-14-00158.1

Vigh, J., & Schubert, W. H. (2009). Rapid development of the tropical cyclone warm core. *Journal of the Atmospheric Sciences*, *66*(11), 3335–3350. https://doi.org/10.1175/2009JAS3092.1

Wang, J., & Coauthors (2015). A long-term, high-quality, high-vertical-resolution GPS Dropsonde dataset for hurricane and other studies. *Bulletin of the American Meteorological Society*, *96*(6), 961–973. https://doi.org/10.1175/BAMS-D-13-00203.1

Zarzycki, C. M., & Jablonowski, C. (2014). A multidecadal simulation of Atlantic tropical cyclones using a variable-resolution global atmospheric general circulation model. *Journal of Advances in Modeling Earth Systems*, *6*, 805–828. https://doi.org/10.1002/2014MS000352

Zhang, J. A., Rogers, R. F., Nolan, D. S., & Marks, F. D. (2011). On the characteristic height scales of the hurricane boundary layer. *Monthly Weather Review*, *139*(8), 2523–2535. https://doi.org/10.1175/MWR-D-10-05017.1

Zhao, M., Golaz, J.-C., Held, I. M., Ramaswamy, V., Lin, S.-J., Ming, Y., et al. (2016). Uncertainty in model climate sensitivity traced to representations of cumulus precipitation microphysics. *Journal of Climate*, *29*(2), 543–560. https://doi.org/10.1175/JCLI-D-15-0191.1

Zhao, M., & Held, I. M. (2012). TC-permitting GCM simulations of hurricane frequency response to sea surface temperature anomalies projected for the late 21st century. *Journal of Climate*, *25*(8), 2995–3009. https://doi.org/10.1175/JCLI-D-11-00313.1

Zhao, M., Held, I. M., Lin, S.-J., & Vecchi, G. A. (2009). Simulations of global hurricane climatology, interannual variability, and response to global warming using a 50-km resolution GCM. *Journal of Climate*, *22*(24), 6653–6678. https://doi.org/10.1175/2009JCLI3049.1

Zhao, M., Held, I. M., & Vecchi, G. A. (2010). Retrospective forecasts of the hurricane season using a global atmospheric model assuming persistence of SST anomalies. *Monthly Weather Review*, *138*(10), 3858–3868. https://doi.org/10.1175/2010MWR3366.1